

# Effect of magnetic field distribution on ECR ion source discharge

Yu-Guo Liu<sup>1</sup> · Jian-Lin Ke<sup>1</sup> · Guang-Yi Zhao<sup>1</sup> · Ben-Chao Lou<sup>1</sup> · Yong-Hong Hu<sup>1</sup> · Rong Liu<sup>1</sup>

Received: 20 October 2017 / Revised: 5 January 2018 / Accepted: 12 January 2018 / Published online: 25 July 2018

© Shanghai Institute of Applied Physics, Chinese Academy of Sciences, Chinese Nuclear Society, Science Press China and Springer Nature Singapore Pte Ltd. 2018

**Abstract** An electron cyclotron resonance ion source model that uses a coaxial antenna to inject the RF power was simulated, and the corresponding hydrogen plasma densities of the ion source were calculated at different magnetic field distributions via a fluid model. The results show that most of the microwave power is absorbed around the resonance surface near the antenna when the plasma density is below the cutoff density of  $7.4 \times 10^{16} \text{ m}^{-3}$  for 2.45 GHz microwaves, and the simulation results also show that the plasma density is strongly influenced by the position and shape of the resonance surface, where a larger resonance surface would improve the plasma density.

**Keywords** ECR ion source · Magnetic field distribution · Plasma simulation

## 1 Introduction

The electron cyclotron resonance (ECR) ion source was first proposed by Geller et al. [1] in the late 1960's, and high-current ECR ion sources have been rapidly developed for various purposes since the 1990s [2–6]. The generation and distribution of plasma in an ECR ion source are strongly influenced by the magnetic field distribution, and use of a suitable magnetic field configuration could improve the discharge efficiency [7, 8]. Previous works showed that the beam current of an ECR ion source is

closely related to the axial magnetic field [9, 10], and the optimal magnet configuration is generally represented by a magnetic field distribution along the center axis of the discharge chamber. However, for ion sources with different magnets or solenoids, the optimal magnetic field distributions along the center axis of the discharge chamber may not be the same [2, 6, 10].

Therefore, the influence of the resonance surface on the plasma density rather than the magnet field strength along the center axis of the discharge chamber was studied. An ECR ion source model with a coaxial antenna that injects the RF power was simulated. The hydrogen plasma density of the source was calculated at different magnetic field distributions via a fluid model [11, 12]. The influence of the shape and position of the resonance surface on the plasma density was analyzed.

## 2 The simulation model

Figure 1 shows a schematic of the structure of the simulation model. The time evolution of the microwaves and plasma is simulated in azimuthally symmetric cylindrical coordinates, and the direction of the antenna in the calculation model is along the  $z$ -axis, as shown in Fig. 1. The 2.45 GHz RF power is axially introduced to the discharge chamber via an antenna 8 mm in diameter. The 2D axisymmetric model represents the antenna in the discharge chamber and the permanent ring magnets. The discharge chamber is a cylinder approximately 50 mm in diameter and 50 mm in length. The magnetic field of the ion source is generated by two NdFeB permanent ring magnets, and the direction of magnetization is along the

✉ Yu-Guo Liu  
liuyg10@lzu.edu.cn

<sup>1</sup> Institute of Nuclear Physics and Chemistry, CAEP, Mianyang 621900, China

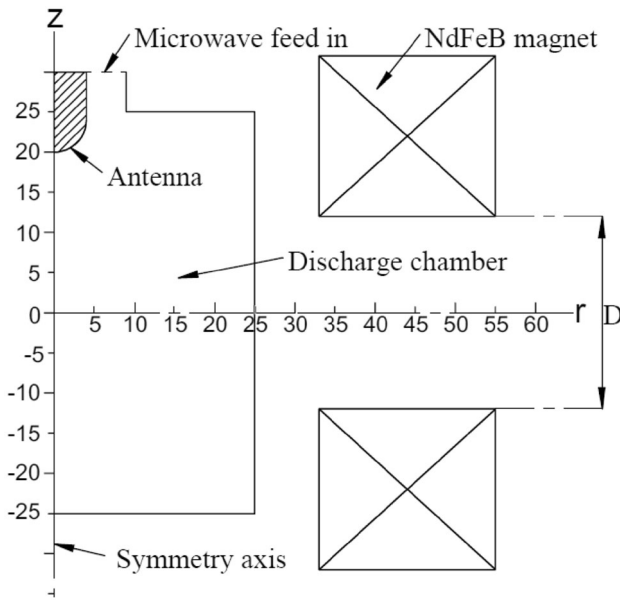


**Fig. 1** Simulation model of the ECR ion source

positive  $z$ -axis. The parameters of the permanent ring magnets are shown in Table 1.

The magnetic field  $\mathbf{B}$  of the permanent ring magnets is obtained by solving the Maxwell–Ampere equations:

$$\nabla \times (\mu_0^{-1} \mu_r^{-1} \mathbf{B}) - \sigma \mathbf{v} \times \mathbf{B} = \mathbf{J}_m, \tag{1}$$

$$\mathbf{B} = \nabla \times \mathbf{A}, \tag{2}$$

where  $\mu$  is the permeability,  $\mathbf{J}_m$  is the azimuthal current at the surface of the ring magnets, and  $\mathbf{A}$  is the magnetic vector potential. The microwave fields were obtained by solving the wave equation:

$$\nabla \times \mu_0^{-1} (\nabla \times \mathbf{E}) - k_0^2 \left( \epsilon_r - \frac{j\sigma}{\omega \epsilon_0} \right) \cdot \mathbf{E} = 0, \tag{3}$$

where  $\mathbf{E}$  is the electric field,  $\mu_0$  is the permeability of free space,  $\epsilon_0$  is the permittivity of free space,  $\epsilon_r$  is the relatively permittivity,  $k_0$  is the wave number,  $\omega$  is the angle frequency of microwave,  $\sigma$  is the full tensor of the plasma conductivity. The electron density  $n_e$  is described by the following equations:

$$\frac{\partial}{\partial t} (n_e) + \nabla \cdot [-n_e (\boldsymbol{\mu}_e \times \mathbf{E}) - T_e \boldsymbol{\mu}_e \cdot \nabla n_e] = R_e, \tag{4}$$

$$\frac{\partial}{\partial t} (n_e) + \nabla \cdot \left[ -n_e \left( \frac{5}{3} \boldsymbol{\mu}_e \cdot \mathbf{E} \right) - T_e \boldsymbol{\mu}_e \times \nabla n_e \right] + \mathbf{E} \times \boldsymbol{\Gamma}_e = R_e, \tag{5}$$

$$\boldsymbol{\Gamma}_e = -n_e \mathbf{E} - T_e \nabla \cdot \boldsymbol{\mu}_e, \tag{6}$$

where  $T_e$  is the electron temperature,  $R_e$  and  $R_e$  are the electron source and energy loss due to inelastic collisions, respectively; and  $\mathbf{E} \cdot \boldsymbol{\Gamma}_e$  is the heating term representing electron motion and heating of electrons by microwaves.  $\boldsymbol{\mu}_e$  is the energy mobility, and  $\boldsymbol{\mu}_e$  is the tensor of the electron mobility.

The working gas is hydrogen in the simulation, and the reaction processes that are taken into account are listed in Table 2. The cross section of each reaction is shown in Fig. 2 [13–15].

### 3 Results and discussion

The typical solution results are shown in Fig. 3, where the gas pressure is 1 Pa, the microwave power is 100 W, and the gap length  $D$  between two permanent ring magnets is 24 mm.

**Table 2** Reactions taken into account in the simulation [13]

Reaction type	Reaction	
Elastic collision	$e + H_2 \rightarrow e + H_2$	(I)
	$e + H \rightarrow e + H$	(II)
Dissociative excitation	$e + H_2 \rightarrow e + H + H$	(III)
	$e + H_2^+ \rightarrow e + H + H^+$	(IV)
	$e + H_3^+ \rightarrow e + 2H + H^+$	(V)
	$e + H^+ \rightarrow e + H + H_2^+$	(VI)
Dissociative combination	$e + H_2^+ \rightarrow H + H$	(VII)
	$e + H_3^+ \rightarrow H + H + H$	(VIII)
Excitation	$e + H \rightarrow e + H^*$	(IX)
$H_3^+$ generation	$H_2 + H_2^+ \rightarrow H_3^+ + H$	(X)
Ionization	$e + H \rightarrow 2e + H^+$	(XI)
	$e + H^* \rightarrow 2e + H^+$	(XII)
	$e + H_2 \rightarrow 2e + H_2^+$	(XIII)
Reaction with wall	$H^+ + \text{wall} \rightarrow 1/2H_2$	
	$H_2^+ + \text{wall} \rightarrow 1/2H_2$	
	$H + \text{wall} \rightarrow 1/2H_2$	
	$H_3^+ + \text{wall} \rightarrow H + H_2$	

**Table 1** Parameters of the permanent ring magnets

Inner diameter (mm)	Outer diameter (mm)	Height (mm)	Remanence (T)	$\mu_r$
66	110	20	1.23	1.05

Figure 3a shows that most of the microwave power is absorbed in the resonance surface ( $B = 875$  G) near the top of the antenna because resonance between the electrons and the microwave field occurs in this region; as a result, the microwave field does most of the work on the electrons to ionize the hydrogen gas near the resonance surface. The corresponding maximum electron density is approximately  $5 \times 10^{16} \text{ m}^{-3}$ , which is below the cutoff density of  $7.4 \times 10^{16} \text{ m}^{-3}$  for 2.45 GHz microwaves [16], and the maximum electron temperature is approximately 10 eV.

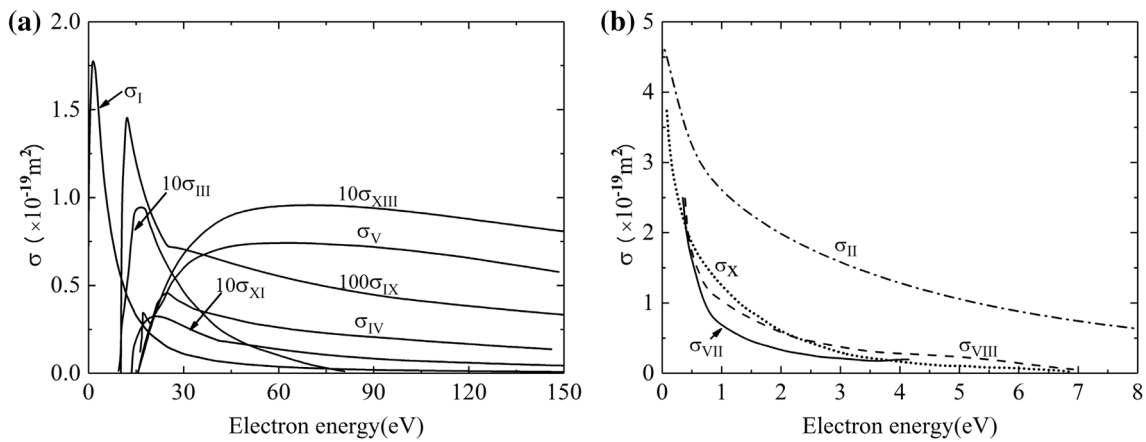
The magnetic field in the discharge chamber could be changed by moving two permanent ring magnets along the  $z$ -axis with a fixed gap length  $D$  or changing the gap length  $D$  between two permanent ring magnets. The magnetic field strength along the source  $z$ -axis for different gap lengths  $D$  is shown in Fig. 4. The minimum magnetic field strength decreases from 1100 to 550 G when the gap length  $D$  increases from 20 to 30 mm, and the corresponding maximum magnetic field strength decreases from 1200 to 1100 G.

The distributions of  $\text{H}^+$  ions and maximum  $\text{H}^+$  ion densities are shown in Figs. 5 and 6, respectively, as the gap length  $D$  increases from 20 to 30 mm.

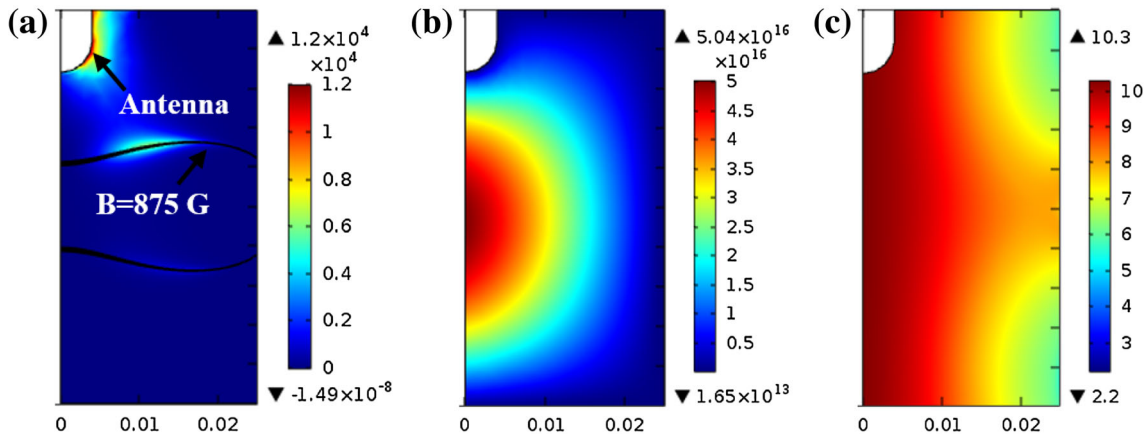
Figure 5 shows that the area of the resonance surface in the discharge chamber is increased with increasing permanent ring magnets gap length  $D$ , and the minimum distance between the antenna and the resonance surface is decreased at the same time.

Figure 6 shows that the maximum density of  $\text{H}^+$  ions first increases with increasing gap length  $D$  and then decreases when  $D$  is larger than 24 mm, and the maximum  $\text{H}^+$  ion density is between  $2.6 \times 10^{16}$  and  $2.8 \times 10^{16} \text{ m}^{-3}$ . In addition, Fig. 6 also shows that the fluctuation of the maximum densities of  $\text{H}_2^+$  ions and  $\text{H}_3^+$  ions is smaller than that of  $\text{H}^+$  ions when the magnet gap length  $D$  is changed.

The distributions of the  $\text{H}^+$  ion densities are also calculated as the ring magnets moved along the  $z$ -axis with a fixed gap length  $D$  of 24 mm; the midpoint of the ring magnets is placed at the origin of the cylindrical coordinates, as shown in Fig. 1, when the corresponding



**Fig. 2** Cross sections of different reactions: **a** cross sections of reaction with high electron energy, **b** cross sections of reaction with low electron energy



**Fig. 3** (Color online) Simulation results: **a** deposited RF power ( $\text{W}/\text{m}^3$ ), **b** electron density ( $\text{m}^{-3}$ ), **c** electron temperature (eV)

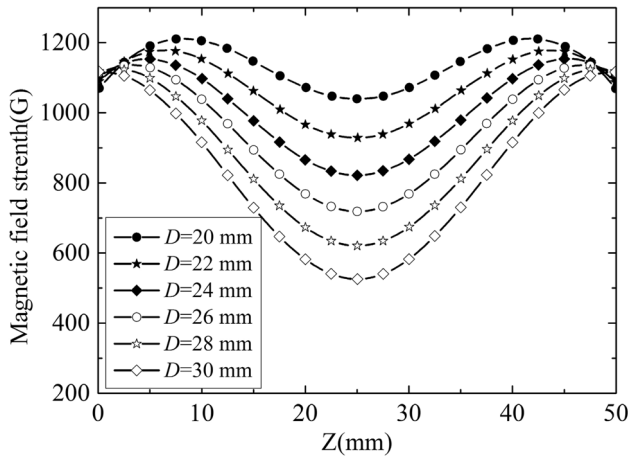


**Fig. 4** Magnetic field strength along the source’s  $z$ -axis for different gap lengths

movement distance  $M$  is zero. The density distributions and the corresponding maximum densities of  $H^+$  ions are shown in Figs. 7 and 8, respectively, as the midpoint of the ring magnets moves along the  $z$ -axis from  $-4$  to  $7$  mm.

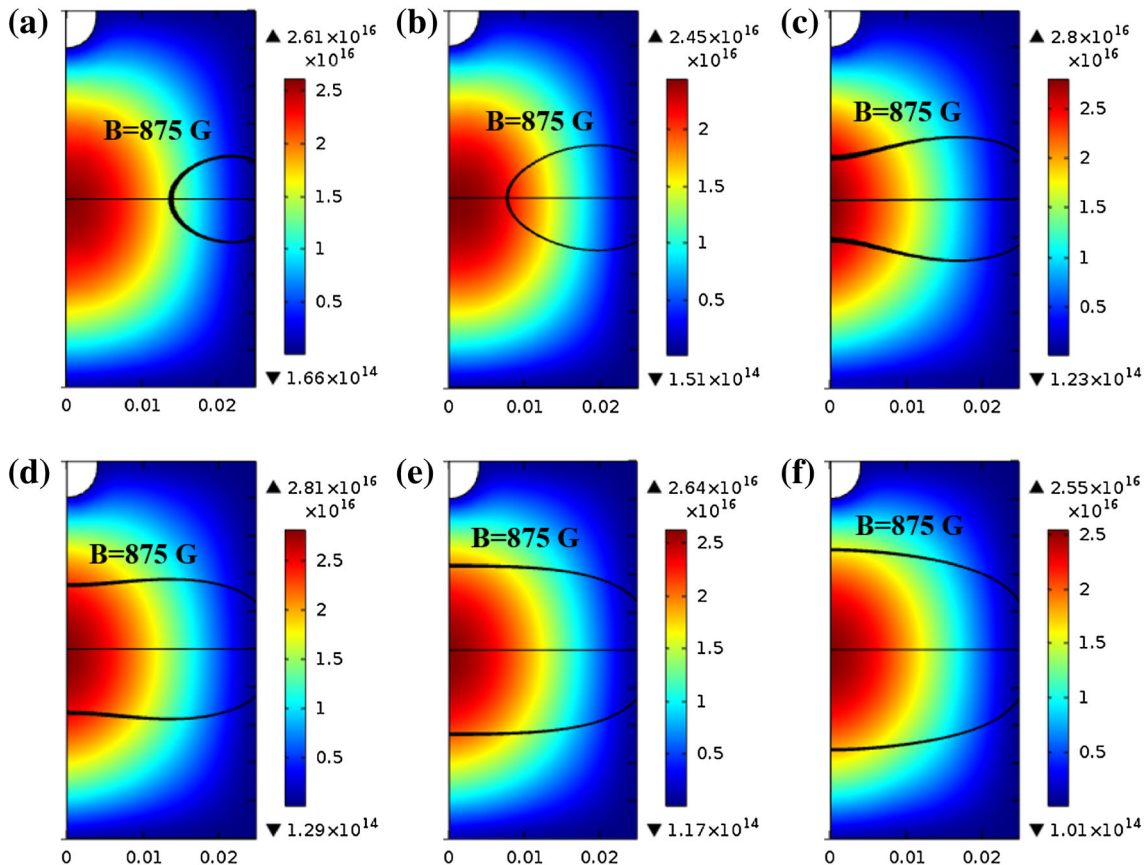
Figure 7 shows that the minimum distance between the antenna and the resonance surface is decreased as the ring magnets move.

Figure 8 shows that the maximum density of  $H^+$  ions is sensitive to the distance between the resonance surface and the antenna. The maximum density of  $H^+$  ions increases from  $2.3 \times 10^{16}$  to  $3.2 \times 10^{16} \text{ m}^{-3}$  when the midpoint of the ring magnets moves along the  $z$ -axis from  $-4$  to  $4$  mm and then decreases to  $2.78 \times 10^{16} \text{ m}^{-3}$  when the midpoint of the ring magnets moves from  $4$  to  $7$  mm along the  $z$ -axis.

The normal electric field component, which is perpendicular to the axial direction, is calculated and shown in Fig. 9, which shows that the normal electric field strength is attenuated exponentially along the  $z$ -axis [17].

The electron density distributions are shown in Fig. 10. Figure 10a shows the electron density distributions along the  $z$ -axis as the ring magnets gap length  $D$  is changed, and Fig. 10b shows the electron density distributions along the  $z$ -axis as the ring magnets move along the  $z$ -axis with a fixed gap length  $D$  of  $24$  mm.

Figure 10 shows that regardless of whether the gap length  $D$  of the ring magnets is changed or the ring magnets



**Fig. 5** (Color online) Density distributions ( $\text{m}^{-3}$ ) of  $H^+$  ions for different magnet gap lengths: **a**  $D = 20$  mm, **b**  $D = 22$  mm, **c**  $D = 24$  mm, **d**  $D = 26$  mm, **e**  $D = 28$  mm, **f**  $D = 30$  mm

are moved along the  $z$ -axis with a fixed gap length  $D$ , the electron density is highest in the central area and then decrease to zero on both sides of the  $z$ -axis.

Figures 5 and 7 show that regardless of whether the gap length  $D$  of the ring magnets is increased or the ring magnets are moved toward the antenna along the  $z$ -axis

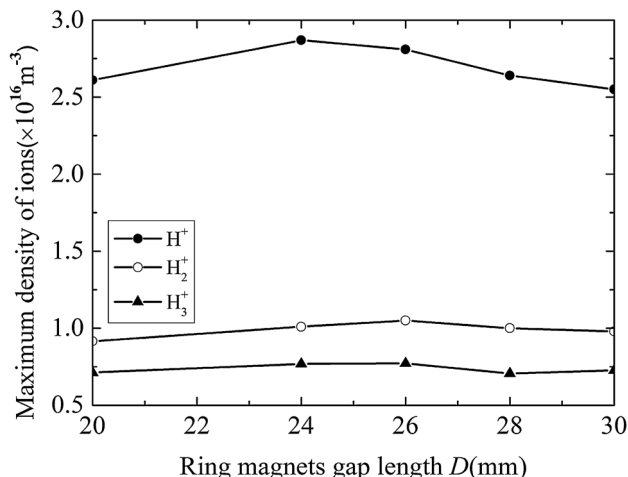


Fig. 6 Maximum density of  $H^+$  ions for different gap lengths  $D$

with a fixed gap length  $D$ , the minimum distance between the resonance surface and the top of the antenna is reduced. Therefore, the normal electric field strength along the  $z$ -axis would increase according to Fig. 9, and the deposited microwave power could be expressed as

$$P = -\frac{e\omega}{2\pi} \int_0^{\frac{2\pi}{\omega}} \mathbf{E} \times \mathbf{v}_e dt, \tag{7}$$

where  $\mathbf{E}$  is the electric field and  $\mathbf{v}_e$  is the electron mean velocity. Consequently the deposited microwave power would increase with decreasing the distance between the resonance surface and the antenna; on the other side, the electron density near the resonance surface would first increase, as shown in Fig. 10, when the distance between the resonance surface and the antenna is reduced. Thus, the density of  $H^+$  ions would increase initially.

When the minimum distance between the resonance surface and the top of the antenna is further reduced, the deposited microwave power near the resonance surface increases continuously as the electron density near the resonance surface decreases. As a result, the number of electrons used to ionize the hydrogen gas decreases, and the density of  $H^+$  ions would decrease as a consequence.

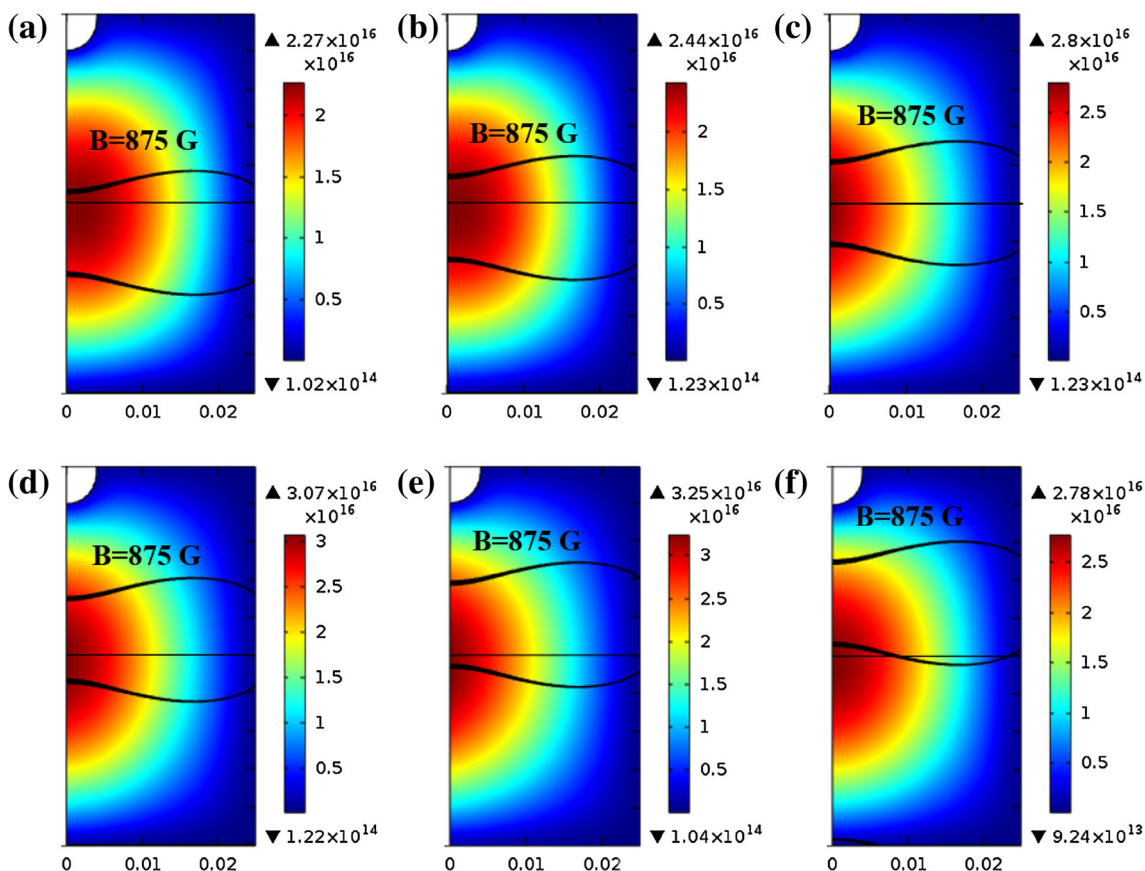
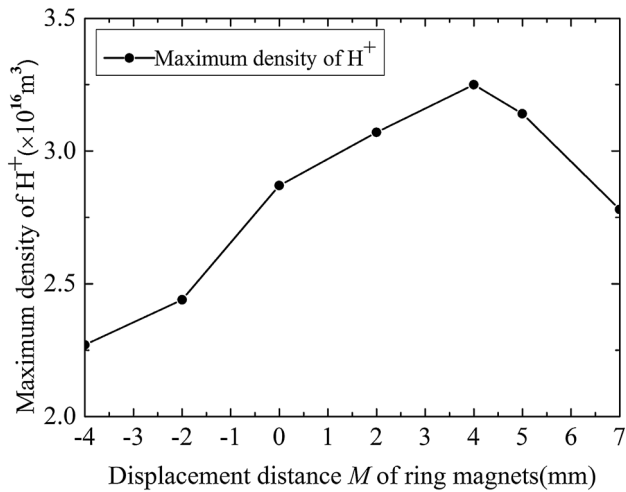
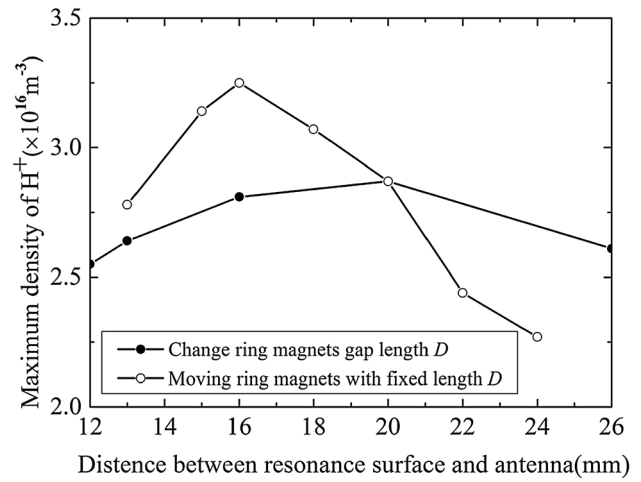


Fig. 7 (Color online) Distributions of  $H^+$  ions ( $\text{m}^{-3}$ ) for different ring magnets position: a  $M = 20$  mm, b  $M = 22$  mm, c  $M = 24$  mm, d  $M = 26$  mm, e  $M = 28$  mm, f  $M = 30$  mm



**Fig. 8** Maximum density of  $H^+$  ions for different distances between the resonance surface and antenna



**Fig. 11** Maximum density of  $H^+$  ions for different resonance surface positions

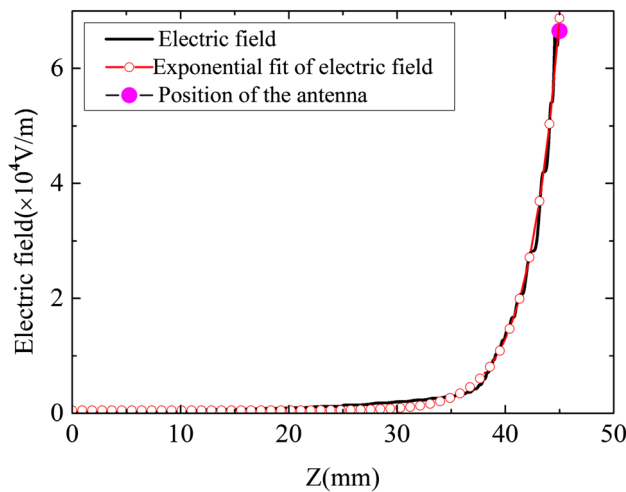


**Fig. 9** Normal electric field that perpendicular to the axial direction

Therefore, the graphs in Figs. 6 and 8 both have a tendency to rise initially and then fall. However, the shape of the resonance surface also changes with increasing ring magnets gap length  $D$ , which may be the main reason for the discrepancy between Figs. 6 and 8.

The maximum density of  $H^+$  ions under different magnetic field distributions, which was obtained by replacing the abscissas of Figs. 6 and 8, with the minimum distance between the resonance surface and the top of the antenna is shown in Fig. 11.

Figure 11 shows that the maximum density of  $H^+$  ions has a tendency to rise at first and then fall when the minimum distance between the resonance surface and the antenna is reduced. Further, the maximum  $H^+$  ions densities under the same abscissa values are not equal in Fig. 11; the variation of the  $H^+$  ion density caused by moving the magnets rings with a fixed gap length  $D$  is larger than

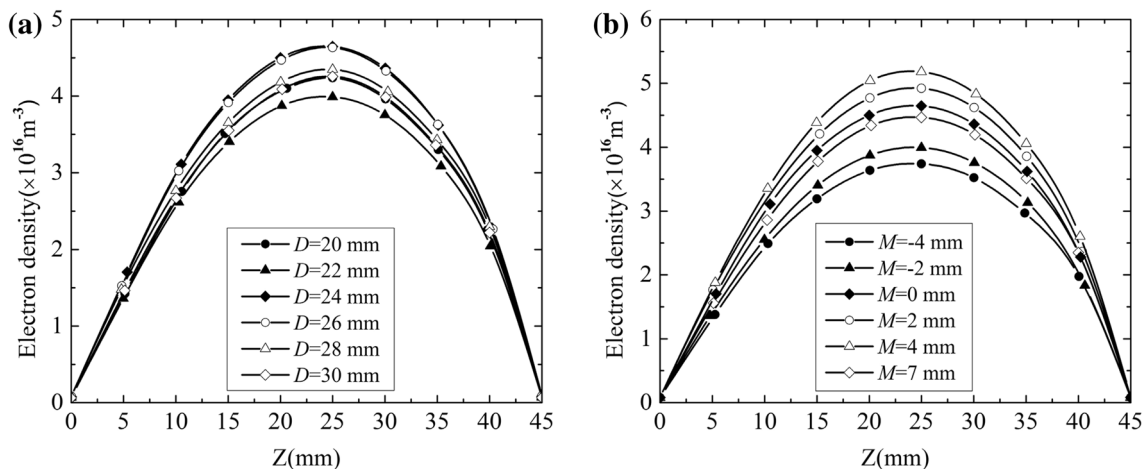


**Fig. 10** Electron density distributions along the  $z$ -axis: **a** ring magnets gap length  $D$  was changed, **b** ring magnets move along the  $z$ -axis with a fixed gap length  $D$  of 24 mm

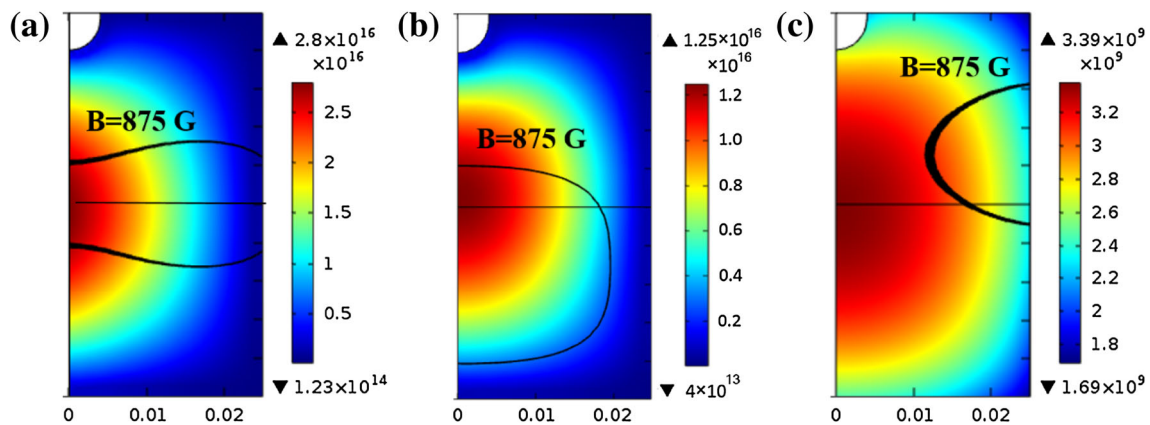


**Fig. 12** (Color online)  $H^+$  ion density distributions ( $m^{-3}$ ) for the different resonance surface shapes: **a** shape A, **b** shape B, **c** shape C

changing the ring magnets gap length  $D$ , indicating that the maximum  $H^+$  ion density is associated with not only the position but also the shape of the resonance surface.

The distributions of the  $H^+$  ion density under different resonance surface shapes are shown in Fig. 12, where the resonance surface shapes were changed by adjusting the size and gap length of the magnets. The minimum distance between the resonance surface and the antenna is 15 mm as the ring magnets are moved along the  $z$ -axis.

The maximum  $H^+$  ion density in Fig. 12a is  $2.8 \times 10^{16} m^{-3}$  and that in Fig. 12b is  $1.25 \times 10^{16} m^{-3}$ , whereas that in Fig. 12c is only  $3.39 \times 10^9 m^{-3}$ . Although the minimum distance between the resonance surface and the top of the antenna is the same in each figure, the corresponding  $H^+$  ion density is quite different. The resonance surface in Fig. 12c is located at the side of the discharge chamber, and the resonance surface area is also smallest compared with those in the other figures; therefore, the  $H^+$  ion density is lowest in Fig. 12c. The resonance surfaces in Fig. 12a, b are both located in the center of the discharge chamber; however, the resonance surface area in Fig. 12a is larger than that in Fig. 12b. As a result, the maximum  $H^+$  ion density of Fig. 12a is approximately twice that in Fig. 12b. This result shows that the area of the resonance surface has an important effect on the  $H^+$  ion density; a large flat resonance surface would improve the  $H^+$  ion density.

## 4 Conclusion

A permanent magnet ECR ion source model was simulated via a fluid model using hydrogen as the working gas. The simulation results show that the maximum electron density is approximately  $5 \times 10^{16} m^{-3}$ , and the maximum electron temperature is approximately 10 eV.

The simulation results also show that the most of the microwave power is deposited around the resonance surface near the antenna when the plasma density is below the cutoff density ( $7.4 \times 10^{16} m^{-3}$ ) for 2.45 GHz microwaves. The  $H^+$  ion densities under different magnetic field configurations were calculated; the results show that the  $H^+$  ion density is strongly influenced by the shape and position of the resonance surface. The  $H^+$  ion density is sensitive to the distance between the antenna and the resonance surface, and a larger resonance surface would improve the  $H^+$  ion density.

## References

1. R. Geller, B. Jacquot, C. Jacquot, Suppression of instabilities and collision limited plasma accumulation in the pleiade mirror device. *Phys. Lett. A* **30**, 80–81 (1969). [https://doi.org/10.1016/0375-9601\(69\)91146-3](https://doi.org/10.1016/0375-9601(69)91146-3)
2. J. Sherman, A. Arvin, L. Hansborough et al., Development of a 130-mA, 75-kV high voltage column for high-intensity dc proton injectors. *Rev. Sci. Instrum.* **69**, 1017–1019 (1998). <https://doi.org/10.1063/1.1148707>
3. M. Delaunay, E. Touchais, Electron cyclotron resonance plasma ion source for material depositions. *Rev. Sci. Instrum.* **69**, 2320–2324 (1998). <https://doi.org/10.1063/1.1148938>
4. R. Gobin, P.Y. Beauvais, D. Bogard et al., High intensity ECR ion source ( $H^+$ ,  $D^+$ ,  $H^-$ ) developments at CEA/Saclay. *Rev. Sci. Instrum.* **73**, 922–924 (2002). <https://doi.org/10.1063/1.1428783>
5. B. Cui, R. Wang, Y. Ma et al., A high intensity microwave ion source for high current RFQ. *Rev. Sci. Instrum.* **75**, 1457–1459 (2004). <https://doi.org/10.1063/1.1690460>
6. Z.Z. Song, S.X. Peng, J.X. Yu et al., Minipermanent magnet high-current microwave ion source. *Rev. Sci. Instrum.* **77**, 03A305-1–03A305-3 (2006). <https://doi.org/10.1063/1.2150807>
7. O.A. Popov, Effects of magnetic field and microwave power on electron cyclotron resonance-type plasma characteristics. *J. Vac. Sci. Technol. A* **9**, 711–716 (1991). <https://doi.org/10.1116/1.577349>

8. T. Taylor, J.F. Mouris, An advanced high-current low-emittance dc microwave proton Source. *Nucl. Instrum. Method. A* **336**, 1–5 (1993). [https://doi.org/10.1016/0168-9002\(93\)91074-W](https://doi.org/10.1016/0168-9002(93)91074-W)
9. J.S.C. Wills, R.A. Lewis, J. Diserens et al., A compact high-current microwave-driven ion source. *Rev. Sci. Instrum.* **69**, 65–68 (1998). <https://doi.org/10.1063/1.1148479>
10. S.X. Peng, R. Xu, J. Zhao et al., The influence of magnetic field configuration on an electron cyclotron resonance ion source a. *Rev. Sci. Instrum.* **79**, 02A310 (2008). <https://doi.org/10.1063/1.2812343>
11. G.J.M. Hagelaar, K. Makasheva, L. Garrigues, Boeuf, Modelling of a dipolar microwave plasma sustained by electron cyclotron resonance. *J. Phys. D Appl. Phys.* **42**, 1–12 (2009). <https://doi.org/10.1088/0022-3727/42/19/194019>
12. D. Hemmers, M. David, H. Kempkens et al., Self-consistent modelling of overdense plasmas in ECR discharges. *J. Phys. D Appl. Phys.* **31**, 2155–2164 (1998). <https://doi.org/10.1088/0022-3727/31/17/013>
13. H. Zhang, C. Wan, *Ion Source and High Power Neutral Beam Source* (Atomic Energy Press, Beijing, 1985), pp. 218–221. (in Chinese)
14. [http://jila.colorado.edu/~avp/collision\\_data/electronneutral/ELECTRON.TXT](http://jila.colorado.edu/~avp/collision_data/electronneutral/ELECTRON.TXT)
15. [https://nl.lxcat.net/data/set\\_type.php](https://nl.lxcat.net/data/set_type.php)
16. M.A. Lieberman, A.J. Lichtenberg, *Principles of Plasma Discharge and Materials Processing*, 2nd edn. (John Wiley & Sons, New Jersey, 2005), p. 94
17. M. Feix, Excitation level of plasma oscillations. *Phys. Lett.* **9**, 123–125 (1964). [https://doi.org/10.1016/0031-9163\(64\)90106-4](https://doi.org/10.1016/0031-9163(64)90106-4)